IOPscience iopscience.iop.org

Home Search Collections Journals About Contact us My IOPscience

Additive manufacturing for *in situ* repair of osteochondral defects

This article has been downloaded from IOPscience. Please scroll down to see the full text article.

2010 Biofabrication 2 035004

(http://iopscience.iop.org/1758-5090/2/3/035004)

View the table of contents for this issue, or go to the journal homepage for more

Download details:
IP Address: 172.16.1.138
The article was downloaded on 10/09/2010 at 13:52

Please note that terms and conditions apply.

Biofabrication **2** (2010) 035004 (12pp) doi:10.1088/1758-5082/2/3/035004

Additive manufacturing for *in situ* repair of osteochondral defects

Daniel L Cohen[1], **Jeffrey I Lipton**[1], **Lawrence J Bonassar**[1,2] **and Hod Lipson**[1,3,4]

[1] Cornell University, Mechanical and Aerospace Engineering, Ithaca, NY, USA
[2] Cornell University, Biomedical Engineering, Ithaca, NY, USA
[3] Cornell University, Faculty of Computing and Information Science, Ithaca, NY, USA

E-mail: dlc44@cornell.edu, jil26@cornell.edu, lb244@cornell.edu and hod.lipson@cornell.edu

Received 27 April 2010
Accepted for publication 6 August 2010
Published 8 September 2010
Online at stacks.iop.org/BF/2/035004

Abstract
Tissue engineering holds great promise for injury repair and replacement of defective body parts. While a number of techniques exist for creating living biological constructs *in vitro*, none have been demonstrated for *in situ* repair. Using novel geometric feedback-based approaches and through development of appropriate printing-material combinations, we demonstrate the *in situ* repair of both chondral and osteochondral defects that mimic naturally occurring pathologies. A calf femur was mounted in a custom jig and held within a robocasting-based additive manufacturing (AM) system. Two defects were induced: one a cartilage-only representation of a grade IV chondral lesion and the other a two-material bone and cartilage fracture of the femoral condyle. Alginate hydrogel was used for the repair of cartilage; a novel formulation of demineralized bone matrix was used for bone repair. Repair prints for both defects had mean surface errors less than 0.1 mm. For the chondral defect, 42.8 $\pm$ 2.6% of the surface points had errors that were within a clinically acceptable error range; however, with 1 mm path planning shift, an estimated $\sim$75% of surface points could likely fall within the benchmark envelope. For the osteochondral defect, 83.6 $\pm$ 2.7% of surface points had errors that were within clinically acceptable limits. In addition to implications for minimally invasive AM-based clinical treatments, these proof-of-concept prints are some of the only *in situ* demonstrations to-date, wherein the substrate geometry was unknown *a priori*. The work presented herein demonstrates *in situ* AM, suggests potential biomedical applications and also explores *in situ*-specific issues, including geometric feedback, material selection and novel path planning techniques.

(Some figures in this article are in colour only in the electronic version)

1. Introduction

Tissue engineering (TE) has the potential to fundamentally change medical practice by addressing donor supply and organ rejection issues. In particular, TE has been demonstrated for creation of living cartilage [1–8] and bone [9, 10] constructs in anatomical shapes. Various techniques for achieving geometric complexity have been employed, including the layering of cells [11], layering of cell-seeded hydrogels [12, 13], casting of seeded hydrogels onto complex surfaces [14], seeding of molded porous scaffolds [15] and injection molding of seeded hydrogels [16]. None of these techniques, however, enables the fabrication of constructs with multi-axial spatial heterogeneities, including different cell types or densities. Furthermore, these techniques require custom tooling, and consequently, achieving patient-specific shapes is non-trivial and sometimes prohibitively challenging. One approach that overcomes these limitations is additive manufacturing (AM) of cell-seeded hydrogels. Toward this end, a number of techniques have recently emerged, including AM of photocrosslinkable hydrogels (PEG [17–19]),

[4] Author to whom any correspondence should be addressed.

 © 2010 IOP Publishing Ltd Printed in the UK

thermoreversible gels (gelatin [20–25], pluronic [26], collagen [21, 26, 27]) and post-deposition ionically crosslinked alginate hydrogel [24, 25, 28].

These AM techniques, however, have only been demonstrated for the fabrication of TE constructs *in vitro*. That is, none of these techniques have been employed *in situ* [29–31] directly on a wound site. Moreover, these approaches are not amenable to *in situ* AM because they rely on external environmental cues, such as UV light, temperature and calcium availability to initiate the phase change after deposition. For *in situ* applications, the environment cannot necessarily be controlled, and the introduction of precise external environmental cues within the body is likely unfeasible. One technique, however, the deposition of alginate hydrogel with ionic crosslinking initiated prior to deposition [32], does not rely upon external cues for phase change after deposition, and thus is compatible with *in situ* applications. In addition to finding compatible materials, other issues needed to be addressed to enable *in situ* repair, such as imaging, registration and path planning.

Even beyond the medical context, *in situ* AM has only rarely been demonstrated, and never in a generalized context without *a priori* substrate-shape information, as conducted herein. *In situ* AM of thermocouples [30] and wire networks [33] has been demonstrated onto pre-existing objects of complex geometry; however, in both of these cases the geometry was known, i.e. hard-coded into the planning sequence. Generalized *in situ* AM, although potentially powerful, has likely been hampered by the lack of pre-existing geometric feedback-based AM techniques/algorithms. Prior to this work, geometric feedback has only been used in limited cases, such as stabilizing AM process parameters [34–36] and individual droplet shapes [37]. However, geometric feedback had never been used for ascertaining substrate geometry in order to print onto pre-existing objects of unspecified shape. Furthermore, no techniques had been developed to handle *in situ*-specific challenges, including path planning, materials formulation, image processing and geometric fidelity characterization.

Through the work presented herein, we demonstrated the *in situ* repair of a cylinder-shaped cartilage (i.e. chondral) defect as well as a geometrically complex two-material bone and cartilage (i.e. osteochondral) defect. These defects were created on a calf femur to mimic naturally occurring pathologies. The chondral defect approximated a cylindrical core created by surgeons during the OATS (osteoarticular transfer system) surgical procedure in order to treat a grade IV chondral lesion. The second defect used herein, the osteochondral defect, approximated a severe complex freeform fracture of the femoral condyle in which both bone and cartilage tissues were damaged.

In these cases, the defect-induced femur served as the printing substrate and was mounted in a custom jig within the AM machine. Alginate hydrogel, with ionic crosslinking initiated prior to deposition [32], was used for repair of cartilage; bone was repaired with a novel formulation of demineralized bone matrix (DBM). AM planning was conducted by CT scanning the bone before and after defect creation, differencing of the two images and subsequently raster pathing the resultant geometry. Feature-based image registration was conducted to align the printing substrate within the printer. Herein we demonstrate materials, hardware modifications, CT imaging and registration for the *in situ* repair of both chondral and osteochondral defects.

Potential clinical applications of this *in situ* AM technique are discussed in depth in section 4. These applications include orthopaedic repair that is minimally invasive and/or geometrically patient-specific. With other material sets and the appropriate seeded cells, this approach could potentially be extended to fields such as facial reconstruction and general trauma surgery.

2. Materials and methods

2.1. Alginate hydrogel preparation

Alginate hydrogels were prepared for printing, using techniques based on those described previously [32]. The alginate solution was created by mixing low-viscosity, high G-content non-medical grade LF10/60 alginate (FMC Biopolymer, Drammen, Norway) with PBS at a concentration of 20 mg mL^{-1}. The $CaSO_4$ crosslinker solution was created at a concentration of 10 mg mL^{-1} in PBS. The alginate and crosslinker solutions were combined in a 2:1 ratio and mixed 150 times through a stopcock at 1 Hz. The mixed alginate hydrogel was loaded into a 10 mL syringe (EFD Inc., East Providence, RI) and allowed to cure for at least 10 min before use in any printing or experimentation.

2.2. Demineralized bone matrix paste preparation

The basis of the printable bone paste was demineralized bone matrix (DBM) in a purified powdered gelatin carrier (BioSet™; Regeneration Technologies Inc., Alachua, FL). The manufacturer specifies 38% Bioset DBM-gelatin powder in water by weight. The paste is prepared by mixing the Bioset DBM-gelatin powder with water through a two-port Luer-lok connector by walking the syringes back-and-forth in unison ten times. Even though the largest standard-diameter deposition tip of the AM machine (1.50 mm diameter × 12 mm long straight barrel) was used for initial material calibration, the DBM paste was still too viscous to be extruded. If the tip were any larger, even though it would reduce the associated extrusion force, the resultant print resolution would be inadequate for the repair of millimeter-scale defects.

We conducted a material tuning experiment in order to find an appropriate powder–water composition that was low viscosity enough for extrusion but high viscosity enough for the printed material to retain its shape post-deposition. Three formulations were tested: the manufacturer-specified formulation (38% DBM-gelatin powder in water by weight) and two others with higher concentrations of water (34% and 30% DBM-gelatin powder in water by weight). Three properties were measured for each tested formulation: minimum extrusion force, sag and work life.

The minimum extrusion force was the force required to induce material flow through the deposition tip. The

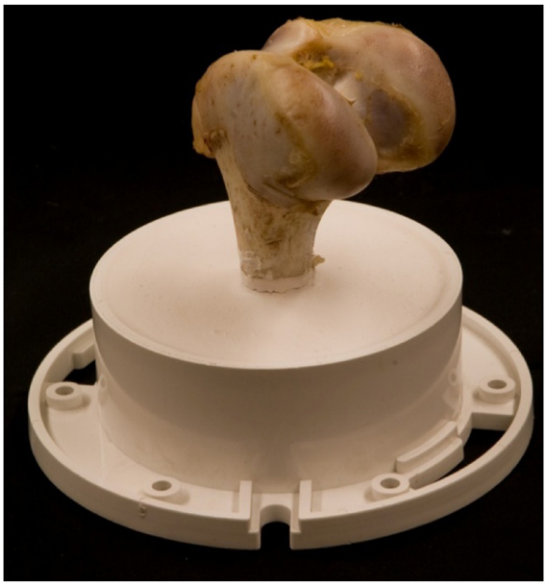


Figure 1. Femoral printing substrate. The femur was set vertically into a plastic pipe fitting. The pipe fitting screwed directly into the printer's hot-swappable base tray.

AM machine's material bay (i.e. a disposable syringe, see section 2.6) was loaded with paste, held vertically on a digital scale and the force at which flow began was recorded. Sag was determined by manually extruding 10 mm tall, 6 mm diameter cylinders and measuring the height difference over the first 15 min. Work life was determined by measuring the elapsed time before the previously determined minimum extrusion force no longer induced paste flow.

2.3. Harvest and preparation of the femoral printing substrate

The printing substrate for the experiments presented herein was the distal end of a bovine femur. The leg of a sacrificed 1- to 3-day-old calf was dissected to isolate the femur. Muscular and connective tissues were removed while maintaining the geometric integrity of the femoral condyles. The isolated femur was placed in boiling water for 20 min in order to preserve the bone. The femur was then cut halfway down the shaft and vertically set in molding plaster (US Gypsum Company, Chicago, IL) within a PVC flange (figure 1). The bone–flange assembly was mounted on a removable acrylic tray and inserted into the printer.

2.4. CT imaging of the femoral printing substrate

CT images were collected on a 16-slice Toshiba Aquilion LB. Volumetric data were collected in 0.5 mm segments and reconstructed using standard Toshiba-CT bone and soft tissue algorithms (figure 2).

2.5. Creation of defects in the femoral condyles

Defects were created on the surface of the femoral printing substrate by a veterinary orthopaedic surgeon to mimic pathological cases. Two of these defects were used for printing experimentation (figure 3). The first induced defect, herein referred to as 'case 1' or the 'chondral defect', simulated a grade IV lesion of the articular cartilage on the medial femoral condyle (figure 4). A grade IV lesion is one in which the tear of the cartilage goes all the way down to the underlying bone surface, but does not extend into the bone. In order to create this defect, a 16 mm diameter circular punch was used to core out the condyle ∼4 mm downward to the bone surface.

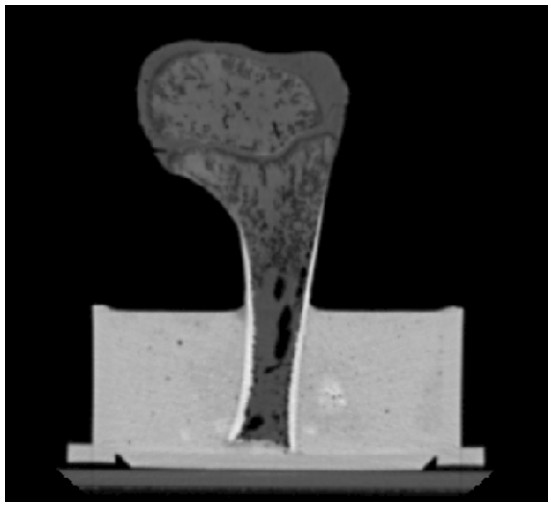


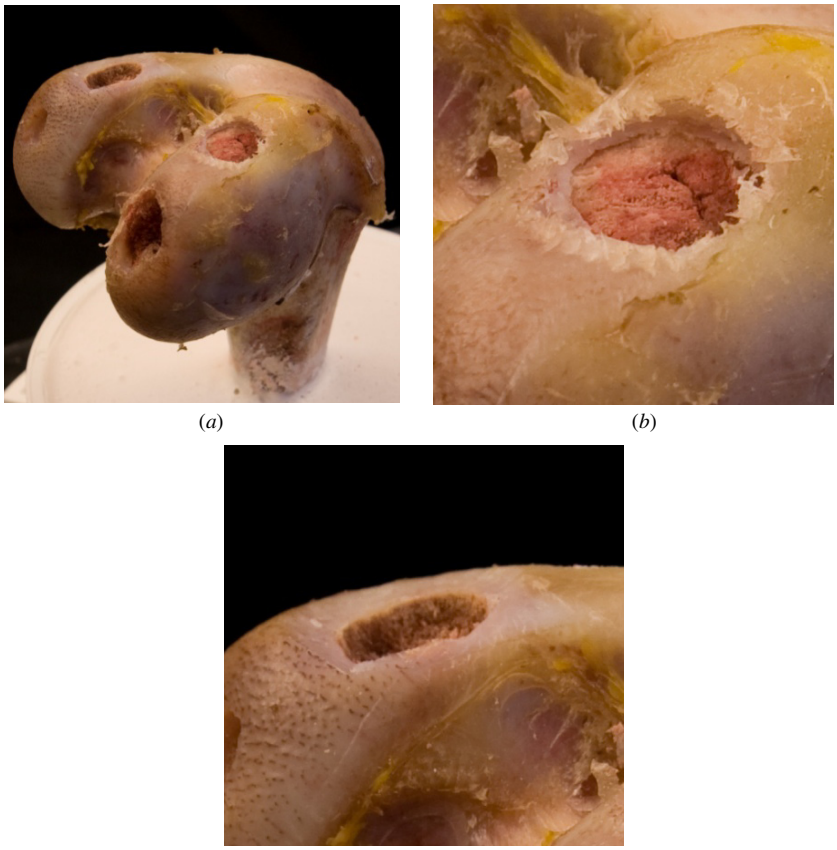
Figure 2. CT image of the femur and its mounting jig.

The second defect, herein referred to as 'case 2' or the 'osteochondral defect', was a first-order approximation of a fracture in which a portion of the lateral femoral condyle sheared off (figure 4). In the severe fracture scenario, the cartilage cap breaks off as well as some of the underlying bone tissue. This two-tissue defect was created by using a scalpel to slice transversely to the condyle. The cut was made ∼4 down from the distal end of the condyle and extended ∼1 mm down into the underlying bone. To increase the severity of the simulated injury, the bone tissue was further resected with a curette by carving out a ∼4 mm deep dome-shaped cavity.

2.6. Additive manufacturing system

A Fab@Home open-source, open-architecture AM system was used for the experiments presented herein [38] (figure 5). This system, which was designed and deployed by our lab, comprised a laser cut acrylic chassis with a three-axis gantry motion system. Each axis was belt-driven and actuated by Snap Motors™, which are dc-geared servo motors (JR Kerr LLC., Berkeley, CA). Communication and motion was coordinated by a USB-interfaced Snap Hub™, which is part of the Snap Motor™ system (JR Kerr LLC, Berkeley, CA). The open-source control software was written by our lab, and, along with the hardware design files, is freely available at www.fabathome.org.

The standard Fab@Home design was modified in order to allow for easy swapping of the printing substrate. The Fab@Home's traditional base was upgraded to a custom



(*a*) (*b*)

(*c*)

Figure 3. Femoral printing substrate with induced chondral and osteochondral defects. (*a*) Overview of four defect sites. Two of these sites were used for experimentation. (*b*) Close-up view of chondral defect site. A cartilage disc was removed exposing the underlying bone surface. (*c*) Close-up view of osteochondral defect site. A bone sliver was removed and the underlying bone was also cored out.

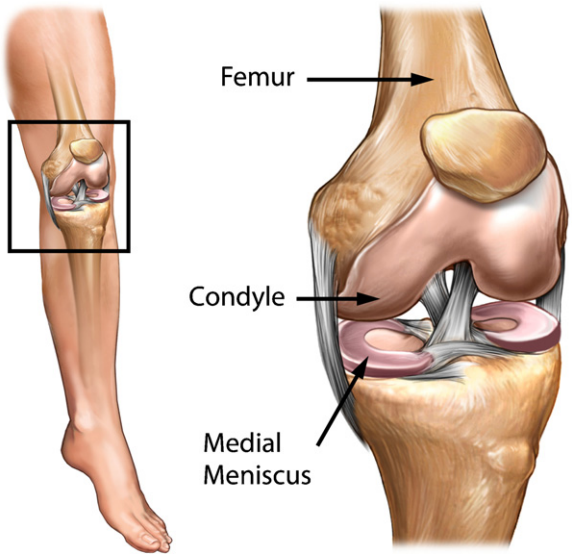


Figure 4. Diagram of knee anatomy. The femur bears substantial load during normal usage. Chondral lesions and osteochondral fractures could potentially develop on the femur–tibia interface. Medical Illustration Copyright © 2010 Nucleus Medical Media, All Rights Reserved. www.nucleusinc.com

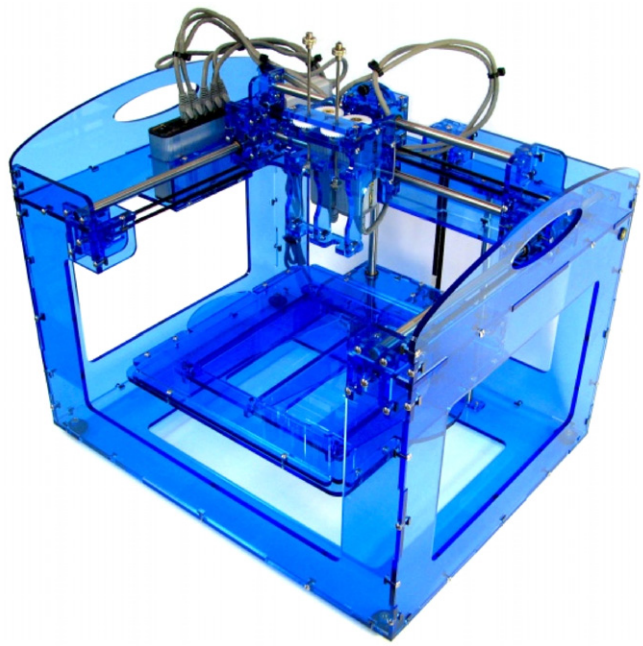


Figure 5. Fab@Home AM system. The Fab@Home AM system is an open-source, open-architecture platform. The material-filled syringes insert into the deposition tool, and a servo motor pushes upon the plunger to extrude material through the Luer-lok tip.

hot-swappable cartridge-style base plate (figure 6). Acrylic trays, 190 mm by 225 mm, were placed in the recess of

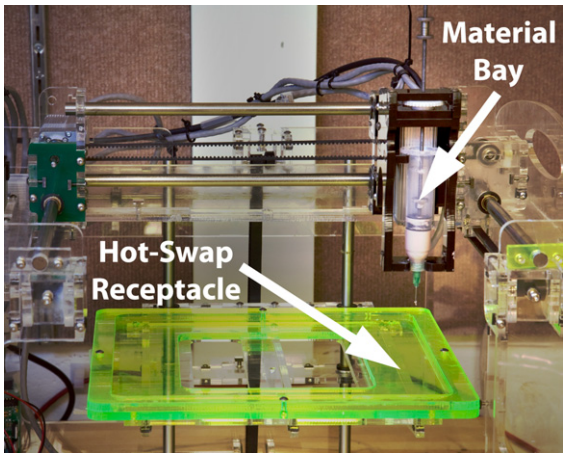


Figure 6. The standard base plate was modified to accommodate hot-swappable snap-in trays. The easy removal of printing parts is an important feature for enablement of *in situ* printing. Once the part is registered, if the machine needed to be serviced, the removable tray allowed for service without registration loss.

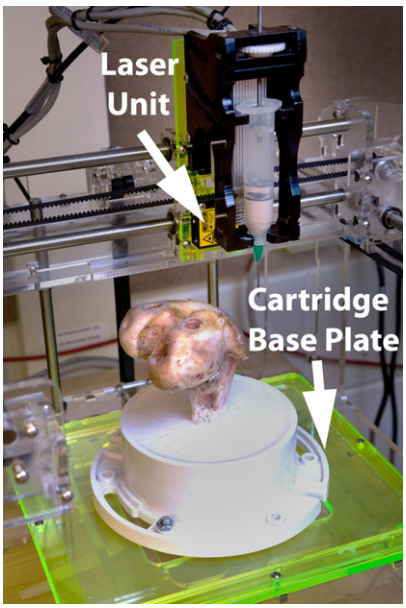


Figure 7. The laser distance sensor was mounted behind the deposition tool.

the Fab@Home's modified base plate and secured by an interference fit. This feature is an important adaptation for *in situ* AM applications as it enables parts to be removed for inspection and replaced without the loss of spatial registration.

Another modification was made to accommodate a laser distance sensor (OADM12 Laser; Baumer Ltd, Southington, CT). The laser sensor was mounted in between the *Y*-axis carriage and the deposition tool (figure 7). This sensor had a 104 mm range and a distance measurement resolution of 0.12 mm. The laser was used for measuring the geometric fidelity of printed constructs post-print by scanning the printer workspace.

2.7. *Path planning for* in situ *AM*

The CT images of the femoral printing substrate were used for AM path planning. One CT scan before the creation of the defects and a second scan afterward were imported in Mimics V12 (Materialise Group, Leuven, Belgium) as DICOM files and converted into 3D solid models. More specifically, during this conversion, the bone and cartilage tissues were isolated by creating a mask that thresholded the intensity values between −906 and 3071 Hounsfields, which corresponded to the tissues of interest. These values were determined by iteratively modifying the intensity thresholds and ensuring complete inclusion of the target constructs while exclusion of background noise, such as out-of-scope tissues and environmental features. To further remove image noise, a region-growing algorithm was employed where the femur's centroid served as the seed location and neighboring voxels within the threshold intensity range were included in the data set. The thresholded, region-grown mask was then converted to a 3D mesh, which was exported as an STL file.

A model of the defect was created by applying a Boolean subtraction operator to the 'before' and 'after' STL files. This 'differenced' STL file was imported into the Fab@Home's open-source control software in order to create the path plan of the target print geometry. A layer-wise raster path-planning algorithm was employed. Registration of the femoral printing substrate within the printer was achieved by setting the 3D model's *X*–*Y* origin to the center of a known feature, in this case, the (+*X*, +*Y*) flange mounting bolt. During each print, the laser beam was used to register the coordinate systems by aligning the beam with the known feature (i.e. the bolt) and adding the known *X*–*Y* offset between the laser and deposition tip.

2.8. *Geometric fidelity characterization*

Geometric fidelity was both qualitatively and quantitatively characterized. During visual inspections, key observed characteristics included surface texture, similarity of the overall shape compared to the intended geometry and the presence of point defects such as missing material. In addition to visually inspecting constructs, each printed object was laser scanned (0.3 mm *X*–*Y* resolution, 0.12 mm height resolution). The resultant height data were converted into a 3D solid in Studio V11 (Geomagic Inc., Research Triangle Park, NC) and exported as an STL file. The file was then imported into Qualify V11 (Geomagic Inc., Research Triangle Park, NC) which performed 3D geometric fidelity calculations, comparing the printed geometry to the intended target shape as specified by the CT image of the pre-damage femur. The error calculated was the 3D error between the surface of the actual geometry and the intended geometry (nearest point between the surfaces). Note that all values in this paper are reported as mean ± standard deviation.

2.9. *Benchmarking—determination of clinically allowable geometric errors*

In order to place the measured geometric errors within a clinical context, the repair-print errors were compared to allowable surgical tolerances established in prior literature. Each defect's measured geometric error was compared to tolerances of the medical procedure that best matched

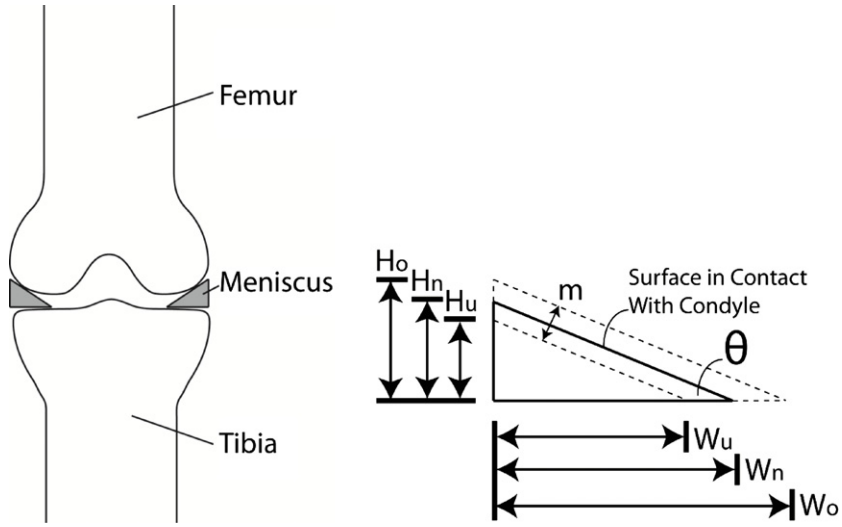


Figure 8. Drawings of femoral condyle and meniscus. (*a*) Femur and tibia with triangular approximation of meniscus in joint. (*b*) Normally sized meniscus [solid line] with over- and under-sized meniscus [dotted lines]. The allowable size variation in the width and height of the meniscus translates into the allowable meniscal–condyle interface deviation, *m*. Note that Hn, Hu and Ho are the normal height, under-sized height and over-sized height, respectively. *Wn*, *Wu* and *Wo* are the normal cross-sectional mediolaterial width, under-sized width and over-sized width, respectively.

the nature of that particular defect. To this end, repair prints of the chondral defect, 'case 1', were compared to tolerances established for the OATS surgical procedure, in which cartilage graft plugs are implanted into manufactured cylindrical defects. Repair prints of the osteochondral defect, 'case 2', were compared to tolerances established for meniscal replacement procedures. Since the meniscus is in direct contact with the condyle (which was repaired in 'case 2'), established tolerances for the sizing of replacement menisci have relevance to benchmarking geometric fidelity for condyle repair.

Several studies have addressed the clinically acceptable geometric tolerances for implantation of cartilage graft plugs in human OATS procedures on the knee [39–41] and ankle [42, 43]. While some surgeons implant the grafts flush with the surface of the surrounding host tissue [40], others prefer to intentionally implant the graft approximately 1 mm above the height of the surrounding host cartilage surface [39, 42, 43]. Although there is no universally accepted graft height-offset, at least one study suggests that as long as the graft is between 0 and 2 mm above the surface of the host tissue, the graft is considered within 'acceptable' geometric tolerances [42]. While 'proud' grafts (i.e. above the host surface) are acceptable, many studies have concluded that grafts implanted beneath the surface of the host tissue are unacceptable as they lead to unfavorable contact forces within the joint [39, 40, 41, 43]. Therefore, for the purposes of benchmarking the 'case 1' repair-print errors, surface points between 0 and 2 mm above the host tissue are considered within an acceptable margin. In addition to reporting the mean geometric error for each sample, the percentage of surface points within the 0 to 2 mm envelope is calculated, as well as the percentage of surface points within the −1 to +1 mm envelope.

Separate criteria were used for benchmarking the geometric errors of the 'case 2' repair prints. To date, no studies have determined acceptable geometric tolerances for freeform condyle repair. However, the condyle is in direct contact with the meniscus, and data do exist for the acceptability of geometric errors in the meniscus [44, 45]. It is assumed herein that geometric tolerances of the meniscal surface are indicative of acceptable tolerances of the condyle since the two parts share the very same interface. That is, if a Q mm error is allowable on the meniscal side of the meniscal–condyle interface, then similarly, a Q mm error is allowable on the condyle side of the meniscal–condyle interface.

More specifically, Dienst *et al* determined that meniscal grafts placed within the human knee closely reproduce normal contact forces as long as the replaced meniscus is within ±10% of the original meniscus geometry [44]. In order to determine how much a 10% error translated to at the meniscal–condyle interface, basic geometric principles were employed. The cross-sectional geometry of the meniscus was assumed to be a triangle (figure 8).

Average human meniscus mediolateral width, *Wn*, is 11.9 ± 2.7 mm [45]. Within the allowable 10% margin established by Dienst *et al*, the range of allowable meniscus width is 10.7 mm (Wu) to 13.1 mm (Wo). Similarly, average meniscus height, *Hn*, is 7.1 ± 1.8 mm [45], yielding an allowable meniscus height of 6.4 mm (Hu) to 7.8 mm (Ho). In order to determine the allowable geometric deviation of the meniscal–condyle interface, one must calculate the difference in the interface position, *m*, between the largest and smallest allowable menisci (figure 8 and equation (1)).

The acceptable geometric deviation of the meniscal–condyle interface is calculated as follows:

$$Wn = 11.9 \pm 2.7 \text{ mm} \quad Wo = 13.1 \text{ mm} \quad Wu = 10.7 \text{ mm}$$
$$Hn = 7.1 \pm 1.8 \text{ mm} \quad Ho = 7.8 \text{ mm} \quad Hu = 6.4 \text{ mm}$$

Table 1. DBM paste characteristics. Printing characteristics of the DBM paste for three different formulations with various concentrations of water, $n = 5$. The pastes were assessed for minimum extrusion force, sag and work life.

Concentration of DBM-Gelatin powder in water by weight (%)	Minimum extrusion force (grams)	Sag (% of initial height)	Work life (minutes)
38	3800 ± 450	3 ± 2	2
34	1900 ± 180	2 ± 2	15
30	740 ± 80	25 ± 8	25

$$m = \cos\phi(Ho - Hu) = \left(\frac{Wn}{\sqrt{Wn^2 + Hn^2}}\right)(Ho - Hu) = 1.2 \text{ mm}. \quad (1)$$

Based on the human meniscus dimensions above, the maximum allowable geometric deviation of the meniscal–condyle interface (i.e. the allowable surface error of the condyle), is an absolute range of 1.2 mm or ±0.6 mm relative to the intended surface (equation (1)). Based on this reasoning, the geometric fidelity criterion for 'case 2', is ±0.6 mm relative to the intended surface.

3. Results

3.1. Tuning of DBM paste formulation

Three different formulations of DBM paste were tested for their printing properties ($n = 5$): 38%, 34% and 30% DBM-gelatin powder in water by weight. The 38% formulation had a minimum extrusion force of 3800 ± 450 grams of force (note: values reported herein are mean ± standard deviation). The 34% and 30% formulations had substantially lower minimum extrusion forces of 1900 ± 180 and 740 ± 80 grams of force, respectively. Only the 34% and 30% formulations fell within the Fab@Home's deposition force limit of ∼2500 grams of force.

The 38% and 34% formulations exhibited similar sag characteristics of 3 ± 2% and 2 ± 2% of the initial part height, respectively. The 30% paste, however, exhibited drastically greater sag at 25 ± 8%. While the sag was recorded over 15 min, the majority of the sagging (most notably for the 30% formulation) occurred within the first 30 s after extrusion.

The work life of the 38% formulation was 2 min. The formulations with higher concentrations of water exhibited extended work lives. The 34% paste had a work life of 15 min and the 30% paste exhibited a work life of approximately 25 min.

The 34% DBM-gelatin powder in water by weight formulation was selected for the subsequent experiments (table 1). This composition yielded the only acceptable combination of minimum extrusion force and material sag. The 38% formulation exceeded the Fab@Home AM system's maximum deposition tool force, while the 30% formulation exhibited unacceptably poor sag characteristics.

3.2. Case 1: chondral defect

The CT scans from before and after the defect creation were processed and differenced in order to create a model of the defect (i.e. the target printing geometry). This geometry was a cylindrical plug that matched the void present in the femoral condyle (figure 9). The 3D model was path-planned in Fab@Home software, and the print was conducted five times to collect sufficient geometric fidelity data.

Alginate hydrogel was used as the ink for the repair of this cartilage-only defect. The gel was printed through a 0.84 mm inner diameter ×31 mm long tapered syringe tip (EFD Inc., East Providence, RI). The printing parameters for alginate were determined through separate calibration experiments in prior work [32]. The key parameters were 0.8 mm path width, 0.71 mm path height and 10 mm s^{-1} deposition tool traverse rate.

The gel construct was printed directly into the defect cavity *in situ* five separate times. After each print, the construct was visually inspected to qualitatively assess geometric fidelity, laser scanned for quantitative analysis, and then the construct was completely removed in preparation for the following print within the same defect-cavity. Across the five prints, the printed alginate hydrogel had a smooth surface texture. Furthermore, the printed geometry closely matched the intended geometry as specified by the CT scan before–after differencing process. The sides of the printed plug were congruent with the perimeter of the induced chondral defect. Also, the top surface of the printed construct matched the contour of the condyle (figure 9).

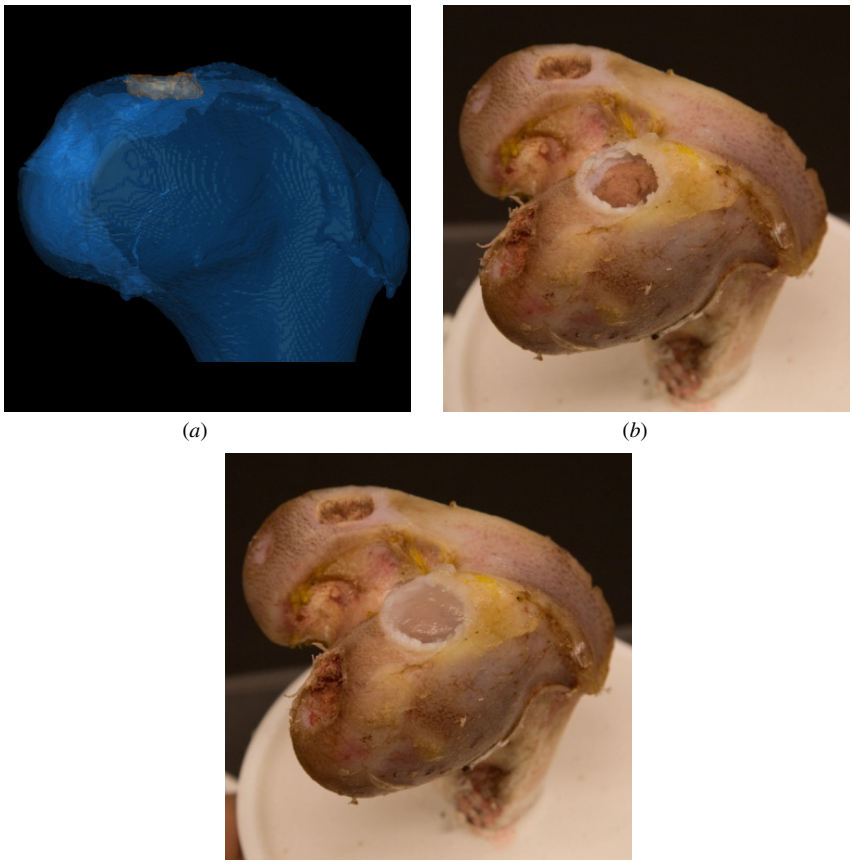
The average of the mean error was 0.0 ± 0.2 mm, $n = 5$ (figure 10). Across the five prints, 42.8 ± 2.6% of the surface points were within the 0 to +2.0 mm error envelope. However, 75.6 ± 7.6% of the surface points fell between −1.0 and +1.0 mm.

3.3. Case 2: osteochondral defect

As in case 1, the CT scans from before and after the defect creation were processed and used for path planning. Unlike case 1, however, the case 2 defect comprised two materials: bone and cartilage. Alginate was again used for cartilage repair; however, the DBM paste was used for the bone portion of the defect.

During path planning, the 3D mesh of the target osteochondral construct was segmented into separate bone and cartilage geometric meshes through manual slicing. This manual slicing process was guided by the CT data which delineated between the two tissues according to the image intensities (related to tissue densities).

The resultant print geometry was a dome-shaped bone plug covered by a cylindrical cartilage cap (figure 11). As before, the alginate hydrogel was printed through a 0.84 mm inner diameter ×31 mm long tapered syringe tip (EFD Inc., East Providence, RI). The same printer parameters were used as in case 1. The DBM paste was printed through a 1.50 mm



(*a*) (*b*)

(*c*)

Figure 9. Repair of chondral defect. (*a*) CT scan of the femur with the chondral defect on the top surface. (*b*) Chondral defect before repair. (*c*) Chondral defect after repair.

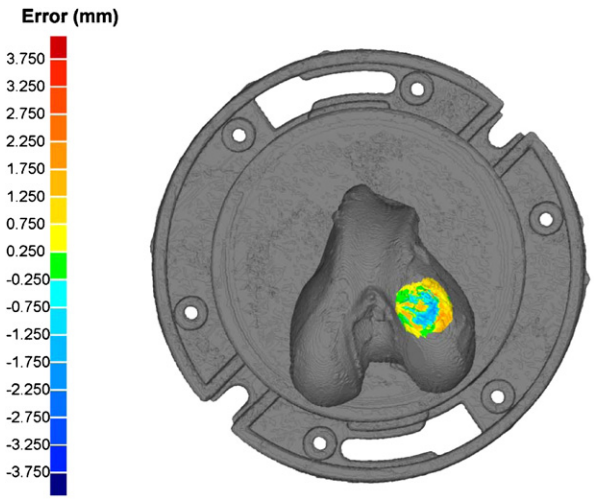
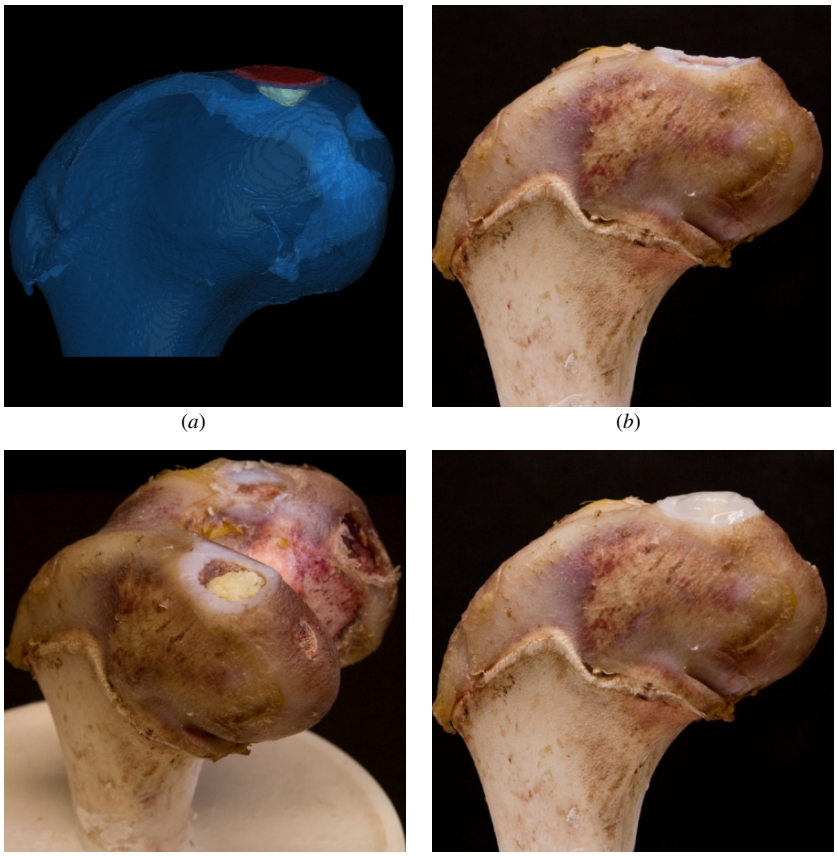


Figure 10. Top-view error plot of chondral defect. The laser scan of the printed surface was compared to the pre-damage CT scan reference geometry. Colors correspond to error magnitude.

diameter ×12 mm long straight-barrel tip (EFD Inc., East Providence, RI), which as described above, was the largest tip that would still provide adequate print resolution. The key printer parameters for the DBM paste were 1.65 mm path width, 1.3 mm path height and 10 mm s^{-1} deposition tool traverse rate. These parameters were determined largely by the selected tip diameter. The specific values were optimized iteratively by fixing the extrusion rate and sweeping through a range of 1–25 mm s^{-1} tool traverse speed until continuous material streams were produced. As in case 1, the print was conducted five times *in situ* to collect geometric fidelity data.

Since this print was an assembly of two constructs, the DBM portion of the print was visually inspected mid-print (i.e. before the alginate deposition). The printed bone construct had a rough surface texture. Its surface profile, however, closely matched the intended surface contour of the substrate's bone tissue. The bone construct was also laterally congruent with the walls of the bone cavity.

Just as in case 1, the print was conducted five separate times within the same defect-cavity. In between prints the geometric fidelity data was captured and then the printed gel was completely removed in preparation for the following print. The printed alginate hydrogel had a smooth surface texture and had a similar geometric fidelity to the alginate prints in case 1. Again, the printed geometry closely matched the intended geometry and the parts were laterally congruent with the defect boundaries. The contour of the 3D freeform alginate construct closely resembled the original pre-defect contour.



(*a*) (*b*) (*c*) (*d*)

Figure 11. Repair of the osteochondral defect. (*a*) CT scan of the femur and the two-material osteochondral defect. The cartilage portion of the defect is highlighted in red and the bone portion in yellow. (*b*) Unrepaired osteochondral defect. (*c*) Partially repaired osteochondral defect where the bone portion has been printed. (*d*) Fully repaired osteochondral defect where the hydrogel is visible and the DBM lays beneath.

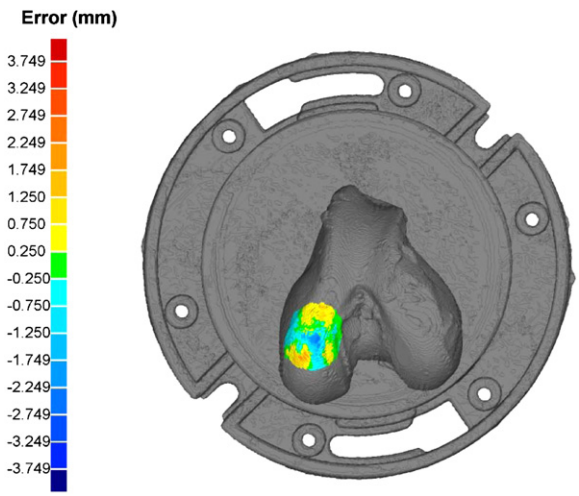


Figure 12. Top-view error plot of osteochondral defect. The laser scan of the printed surface was compared to the pre-damage CT scan reference geometry. Colors correspond to error magnitude.

The average of the mean error was 0.1 ± 0.1 mm, $n = 5$ (figure 12). Across the five prints, 83.6 ± 2.7% of the surface points were within the −0.6 to +0.6 mm error envelope. Moreover, 92.8 ± 3.1% of the points fell within ±1.25 mm of error.

4. Discussion

The two repair prints (‘cases 1’ and ‘2’) exhibited low geometric error in terms of the mean error. The chondral defect repair prints (‘case 1’) and osteochondral defect prints (‘case 2’) had mean errors of less than 0.1 mm. More specifically, the chondral defect had a mean error of 0.0 ± 0.2 mm, and the osteochondral defect had a mean error of 0.1 ± 0.1 mm. These mean errors both fell within the above-established clinical benchmarks of 0 to 2 mm for ‘case 1’, and ±0.6 mm for ‘case 2’.

Upon comparing ‘case 1’ chondral defects to clinical benchmarks, wherein grafts between 0.0 and +2.0 mm are considered acceptable [42], the mean errors fell within the acceptable envelope as noted above. However, in order to more completely analyze the potential efficacy of this technique, the spread of surface point errors must also be addressed. That is, 42.8 ± 2.6% of the surface points were within the 0 to +2.0 mm error envelope. While this at first seems to be somewhat low benchmark-compliance, it should be noted that the print was not conducted with the benchmark in mind. In other words, the geometric path planning was executed with the intended geometry being the exact shape of the original cartilage. If the planning had artificially inserted additional layers to translate the parts 1 mm upward, the

resulting printed constructs would have had mean errors of ∼1 mm (still within the benchmark envelope), yet the spread of points would likely have remained the same. Given that 75.6 ± 7.6% of the surface points fell between −1.0 and +1.0 mm, it can be assumed that if the geometry had been translated upward 1 mm prior to printing, a very similar portion of points would have fallen between the 0 and 2 mm benchmark. Under these assumptions, a benchmark compliance of approximately 75% can likely be achieved with adjusted pre-print planning.

Spread of the surface errors must also be assessed for 'case 2' osteochondral repair prints. Based on the ±0.6 mm envelope [44], 83.6 ± 2.7% of the surface errors fell within acceptable limits. Moreover, if the acceptable bounds were increased to ±1.2 mm, then 92.8 ± 3.1% of the points were within range.

In addition to proposing a methodology for benchmarking *in situ* orthopaedic repair printing, other *in situ*-specific issues were addressed. Perhaps the most critical consideration for *in situ* printing is what types of constraints the deposition techniques and/or materials require post-deposition. For example, stereolithography (SLA) and selective laser sintering (SLS) techniques are not amenable to *in situ* AM since it is not feasible to embed body parts within a liquid vat or powder bed, respectively. Even for techniques which are conceivably amenable, such as robo-casting and direct-writing, material selection must be made carefully. Materials that rely upon post-deposition external environmental cues for phase-change (e.g. temperature fluctuation [20–27], UV light [17, 18, 19], chemical exposure [24, 25, 28]) are not compatible with *in situ* AM since these cues cannot necessarily be reliably introduced within the body during a surgical procedure. For example, in-body AM cannot rely upon the temperature change for the phase change of thermoreversible hydrogels [20–27] since the environmental temperature is dictated by the body and is uncontrollable. Instead, materials must be selected where the phase change was initiated prior to deposition without the need for external cues, such as the pre-crosslinked-alginate [32] and DBM, used herein.

While alginate hydrogel has an established heritage for cartilage TE, we additionally selected DBM for its relevance to bone repair. The novel formulation allows for successful extrusion through a syringe-based deposition tool, yet is geometrically stable after deposition. In order to better understand the efficacy of this approach from a biological perspective, further investigation must be conducted either in culture *in vitro* or perhaps *in vivo*; tissue integration, cell proliferation and extracellular matrix production must all be studied since they have not yet been studied with these materials in this particular context.

Aside from biological considerations and implications of this work, the proof-of-concept work presented herein addresses pressing issues within the broader AM field; these prints are some of the only *in situ* AM demonstrations of any kind to date. *In situ* AM has been demonstrated for fabrication of thermocouples [30] and antennae on helmets [33]; these two examples fit the definition of '*in situ*' in that they were conducted on pre-existing parts of non-flat geometry. In these cases, however, there was no geometric feedback involved and the substrate geometry was hard-coded, and thus, known by the system *a priori*. More generalized *in situ* AM for unknown substrate shapes, based on geometric feedback, has only been conceptualized [29] but never demonstrated. Moreover, geometric feedback has only rarely been used for any purpose in AM. Several groups have employed geometric feedback for quality assurance [34–37, 46], i.e. achieving high geometric fidelity despite process uncertainties, but in these cases they were not printing *in situ* nor accounting for unknown substrate shape. The bone repair prints presented herein used CT-scan-based geometric feedback and novel differencing algorithms to conduct *in situ* prints wherein the complex substrate geometry was unknown *a priori*. Furthermore, we explored associated noise removal techniques, in particular, region growing, which was critical for successfully distilling useful geometric information from differenced medical images. Another *in situ*-specific issue is the registration of the printing substrate within the AM machine; we propose feature-based registration assisted by a laser guide marker. Other possible techniques include automated feature extraction from a pre-print laser scan of the substrate which would be compared to unique features in the medical image data. We also demonstrated *in situ*-specific hardware modifications, such as a deposition-tool-mounted laser sensor and a hot-swappable cartridge-style base plate. These design features are important for both ascertaining geometric data and maintaining proper registration despite potential inspection-related part-removal.

As geometric feedback is harnessed for handling unknown substrate shapes and *in situ* printing is enabled, new paradigms will be created within AM [29]. Rather than replacing parts that have sustained geometrically complex damage, *in situ* AM could be used to salvage these parts. In the biomedical realm, as directly suggested by the proof-of-concept prints conducted herein, *in situ* AM could lead to less invasive clinical treatments. Small incisions could be made to insert a print-head, and in conjunction with CT/MR imaging, damaged body parts could be directly repaired. In the orthopaedic context, the minimally invasive nature of the technique could be leveraged for joint surgeries to repair focal defects or replace larger segments. The technique also could lead to new procedures that push the boundaries of patient-specificity by using advanced medical imaging to drive highly specific repair of anatomical features. Target geometries could be taken from archived pre-damage scans, or they could be based on extrapolations. For example, in cases without the appropriate archived medical data, approximations of the target geometry could be made by applying morphological models to damaged anatomies or by applying symmetry rules and basing the target design off of bilaterally symmetric healthy tissue. By using other print materials and the appropriate seeded cells, this technique could also be extended beyond orthopaedic repair, specifically into the field of facial reconstruction where minimal invasiveness and patient-specificity are particularly important.

It should be noted that process uncertainty will also become more imposing with *in situ* applications. That is, once the printer 'comes to the part' and operates

within the part's environment, it is now beyond the highly controlled environment of traditional AM systems. In addition to unknown substrate geometry, other factors such as uncontrolled humidity, vibration and temperature could potentially lead to adverse effects on the geometric fidelity of the printed part. Thus, geometric feedback is not only important for ascertaining initial substrate geometry and directly enabling *in situ* AM, but also closed-loop techniques may prove critical for ensuring quality despite less controlled environments. The geometric feedback approaches for quality assurance [34–37, 46], mentioned above, will likely become key enablers for the practical implementation of *in situ* AM. Also related to the notion of environmental uncertainty, further investigation must be done to better understand the effect that loads produced by surrounding tissues would have on the repair prints. Stronger materials and/or external patient fixation may be required for clinical implementation of the approach proposed herein.

Through careful selection of printing materials and techniques, novel AM planning sequences, and increasingly accessible imaging modalities, the stage is set for *in situ* to emerge as a new paradigm in AM. In-place repair of systems, ranging from complex machines to human bodies, will benefit from AM operating in the existing parts' own environments. Not only will complexly damaged parts be able to be repaired instead of replaced, but new territories can also be explored toward less invasive repair.

References

[1] Cao Y, Vacanti J P, Paige K T, Upton J and Vacanti C A 1997 Transplantation of chondrocytes utilizing a polymer-cell construct to produce tissue-engineered cartilage in the shape of a human ear *Plast. Reconstr. Surg.* **100** 297

[2] Ibarra C, Jannetta C, Vacanti C A, Cao Y, Kim T H, Upton J and Vacanti J P 1997 Tissue engineered meniscus: a potential new alternative to allogeneic meniscus transplantation *Transplant. Proc.* **29** 986–8

[3] Kamil S H, Kojima K, Vacanti M P, Bonassar L J, Vacanti C A and Eavey R D 2003 *In vitro* tissue engineering to generate a human-sized auricle and nasal tip *Laryngoscope* **113** 90

[4] Kim W S, Vacanti J P, Cima L, Mooney D, Upton J, Puelacher W C and Vacanti C A 1994 Cartilage engineered in predetermined shapes employing cell transplantation on synthetic biodegradable polymers *Plast. Reconstr. Surg.* **94** 233

[5] Kojima K, Bonassar L J, Ignotz R A, Syed K, Cortiella J and Vacanti C A 2003 Comparison of tracheal and nasal chondrocytes for tissue engineering of the trachea *Ann. Thorac. Surg.* **76** 1884

[6] Mizuno H, Roy A K, Vacanti C A, Kojima K, Ueda M and Bonassar L J 2004 Tissue-engineered composites of anulus fibrosus and nucleus pulposus for intervertebral disc replacement *Spine* **29** 1290

[7] Puelacher W C, Mooney D, Langer R, Upton J, Vacanti J P and Vacanti C A 1994 Design of nasoseptal cartilage replacements synthesized from biodegradable polymers and chondrocytes *Biomaterials* **15** 774

[8] Puelacher W C, Wisser J, Vacanti C A, Ferraro N F, Jaramillo D and Vacanti J P 1994 Temporomandibular joint disc replacement made by tissue-engineered growth of cartilage *J. Oral Maxillofac. Surg.* **52** 1172–7

[9] Puelacher W C, Vacanti J P, Ferraro N F, Schloo B and Vacanti C A 1996 Femoral shaft reconstruction using tissue-engineered growth of bone *Int. J. Oral Maxillofac. Surg.* **25** 223–8

[10] Weng Y, Cao Y, Arevalo C, Vacanti M P and Vacanti C A 2001 Tissue-engineered composites of bone and cartilage for mandible condylar reconstruction *J. Oral Maxillofac. Surg.* **59** 185–90

[11] Klein T J, Schumacher B L, Schmidt T A, Li K W, Voegtline M S, Masuda K, Thonar E and Sah R L 2003 Tissue engineering of stratified articular cartilage from chondrocyte subpopulations *Osteoarthritis Cartilage* **11** 595–602

[12] Kim T K, Sharma B, Williams C G, Ruffner M A, Malik A, McFarland E G and Elisseeff J H 2003 Experimental model for cartilage tissue engineering to regenerate the zonal organization of articular cartilage *Osteoarthritis Cartilage* **11** 653–64

[13] Ng K W, Wang C C B, Mauck R L, Kelly T A N, Chahine N O, Costa K D, Ateshian G A and Hung C T 2005 A layered agarose approach to fabricate depth-dependent inhomogeneity in chondrocyte-seeded constructs *J. Orthop. Res.* **23** 134–41

[14] Hung C T, Lima E G, Mauck R L, Taki E, LeRoux M A, Lu H H, Stark R G, Guo X E and Ateshian G A 2003 Anatomically shaped osteochondral constructs for articular cartilage repair *J. Biomech.* **36** 1853–64

[15] Cao Y, Rodriguez A, Vacanti M, Ibarra C, Arevalo C and Vacanti C A 1998 Comparative study of the use of poly (glycolic acid), calcium alginate and pluronics in the engineering of autologous porcine cartilage *J. Biomater. Sci. Polym. Ed.* **9** 475–87

[16] Chang S C, Rowley J A, Tobias G, Genes N G, Roy A K, Mooney D J, Vacanti C A and Bonassar L J 2001 Injection molding of chondrocyte/alginate constructs in the shape of facial implants *J. Biomed. Mater. Res.* **55** 503–11

[17] Albrecht D R, Tsang V L, Sah R L and Bhatia S N 2004 Photo- and electropatterning of hydrogel-encapsulated living cell arrays *Lab Chip* **5** 111–8

[18] Lu Y, Mapili G, Suhali G, Chen S and Roy K 2006 A digital micro-mirror device-based system for the microfabrication of complex, spatially patterned tissue engineering scaffolds *J. Biomed. Mater. Res.* A **77** 396–405

[19] Tsang V L and Bhatia S N 2004 Three-dimensional tissue fabrication *Adv. Drug Deliv. Rev.* **56** 1635–47

[20] Landers R, Hübner U, Schmelzeisen R and Mülhaupt R 2002 Rapid prototyping of scaffolds derived from thermoreversible hydrogels and tailored for applications in tissue engineering *Biomaterials* **23** 4437–47

[21] Landers R, Pfister A, Hübner U, John H, Schmelzeisen R and Mülhaupt R 2002 Fabrication of soft tissue engineering scaffolds by means of rapid prototyping techniques *J. Mater. Sci.* **37** 3107–16

[22] Wang X, Yan Y, Pan Y, Xiong Z, Liu H, Cheng J, Feng L, Feng L, Wu R, Zhang R and Lu Q 2006 Generation of three-dimensional hepatocyte/gelatin structures with rapid prototyping system *Tissue Eng.* **12** 83–90

[23] Wei X, Xiaohong W, Yongnian Y, Wei Z, Zhuo X, Feng L, Rendong W and Renji Z 2007 Rapid prototyping three-dimensional cell/gelatin/fibrinogen constructs for medical regeneration *J. Bioact. Compat. Polym.* **22** 363–77

[24] Yan Y, Wang X, Pan Y, Liu H, Cheng J, Xiong Z, Lin F, Wu R, Zhang R and Lu Q 2005 Fabrication of viable tissue-engineered constructs with 3D cell-assembly technique *Biomaterials* **26** 5864–71

[25] Yan Y, Wang X, Xiong Z, Liu H, Liu F, Lin F, Wu R, Zhang R and Lu Q 2005 Direct construction of a three-dimensional structure with cells and hydrogel *J. Bioact. Compat. Polym.* **20** 259–69

[26] Smith C M, Stone A L, Parkhill R L, Stewart R L, Simpkins M W, Kachurin A M, Warren W L and Williams S K 2004 Three-dimensional Bioassembly tool for generating viable tissue-engineered constructs *Tissue Eng.* **10** 1566–76
[27] Mironov V, Boland T, Trusk T, Forgacs G and Markwald R R 2003 Organ printing: computer-aided jet-based 3D tissue engineering *Trends Biotechnol.* **21** 157–61
[28] Khalil S and Sun W 2009 Bioprinting endothelial cells with alginate for 3D tissue constructs *J. Biomech. Eng.* **131** 1002–8
[29] Pérès F and Noyes D 2006 Envisioning e-logistics developments: making spare parts *in situ* and on demand state-of-the-art and guidelines for future developments *Comput. Ind.* **57** 490–503
[30] Sun L, Jakubenas K J, Crocker J E, Harrison S, Shaw L L and Marcus H L 1998 *In situ* thermocouples in macro-components fabricated using SALD and SALDVI techniques *Mater. Manuf. Process.* **13** 909–19
[31] Whitney E 2004 Advances in rapid prototyping and manufacturing using laser-based solid free-form fabrication *The Handbook of Advanced Materials* (Oak Ridge, TN: Wiley) pp 611–31
[32] Cohen D L, Malone E, Lipson H and Bonassar L J 2006 Direct freeform fabrication of seeded hydrogels in arbitrary geometries *Tissue Eng.* **12** 1325–35
[33] Sampath S 2005 Novel concepts in direct writing of electronics and sensors *Digital Fabrication 2005* (Society for Imaging Science and Technology) pp 21–24
[34] Doumanidis C and Kwak Y-M 2001 Geometry modeling and control by infrared and laser sensing in thermal manufacturing with material deposition *J. Manuf. Sci. Eng.* **123** 45–52
[35] Doumanidis C and Skordeli E 2000 Distributed-parameter modeling for geometry control of manufacturing processes with material deposition *J. Dyn. Syst. Meas. Control* **122** 71–7
[36] Mazumder J, Schifferer A and Choi J 1999 Direct materials deposition: designed macro and microstructure *Mater. Res. Innov.* **3** 118–31
[37] Lovelady M J and Watts J D 1999 Closed loop feedback for continuous mode materials jetting *IEEE/CPMT Int. Electronic Manufacturing Technology Symp. (Austin, TX, 1999)* pp 189–95
[38] Malone E and Lipson H 2007 Fab@Home: the personal desktop fabricator kit *Rapid Prototyping J.* **13** 245–55
[39] Bugbee W D and Convery F R 1999 Osteochondral allograft transplantation *Complex Top. Knee Surg.* **18** 67–75
[40] Hospodar S J and Tokish J M 2005 Management of articular cartilage injuries in the knee *Oper. Tech. Sports Med.* **13** 150–6
[41] Bentley G, Biant L C, Carrington W J, Akmal M, Goldberg A, Williams A M, Skinner J A and Pringle J 2003 A prospective, randomised comparison of autologous chondrocyte implantation versus mosaicplasty for osteochondral defects in the knee *J. Bone Joint Surg.* **85** 223–30
[42] Meehan R E and Brage M E 2004 Fresh osteochondral allografting for osteochondral defects of the talus: a case review *Tech. Foot Ankle Surg.* **3** 53–61
[43] Easley M E and Scranton P E 2003 Osteochondral autologous transfer system *Foot Ankle Clin.* **8** 275–90
[44] Dienst M, Greis P E, Ellis B J, Bachus K N and Burks R T 2007 Effect of lateral meniscal allograft sizing on contact mechanics of the laterial tibial plateau: an experimental study in human cadaveric knee joints *Am. J. Sports Med.* **35** 34–42
[45] Haut T L, Hull M L and Howell T S 2000 Use of roentgenography and magnetic resonance imaging to predict meniscal geometry determined with a three-dimensional coordinate digitizing system *J. Orthop. Res.* **18** 228–37
[46] Cohen D L and Lipson H 2010 Geometric feedback control of discrete-deposition SFF systems *Rapid Prototyping J.* **16** 377–93